



# OPEN Theoretical and experimental study on the thermomechanical characteristics of double-row angular contact automotive wheel bearings

Dong Yanfang<sup>1,2,3,4</sup>✉, He Kai<sup>1</sup>, Qiu Ming<sup>1,2</sup>✉, Yan Zibo<sup>1</sup> & Yu Wei<sup>1</sup>

The thermodynamic characteristics of double-row angular contact wheel bearings are important for the bearing operational condition monitoring and structural design. The load distribution and power consumption distribution of the bearing are obtained by establishing a thermal-force coupling model of the double-row angular contact wheel bearing. Combining with the thermal network and finite element analysis method, the steady-state temperature field of the bearing under test conditions is achieved. Also a box-type encapsulated fiber-optic grating temperature sensor is designed for investigating the effects of working condition parameters on the axial and circumferential temperature distributions of the bearing. And a comparative analysis with the predicted results is carried out. The results show that there are obvious temperature differences in the axial and circumferential direction of double-row angular contact wheel bearing under combined load. The speed, axial force and radial force all affect the bearing temperature rise and temperature distribution.

**Keywords** Double-row angular contact wheel bearings, Thermal coupling, Optical fiber grating sensors, Circumferential temperature difference, Axial temperature difference

Double-row angular contact wheel bearings bear the load from the axle during movement process, reduce relative friction, and assist in movement. The temperature field distribution of wheel bearings is complicated for the harsh service conditions of automobile wheel bearings and the frequent changes in driving conditions. And the thermo-mechanical characteristics of the bearing are crucial, as it is directly impacting the performance and service life of the bearing. An increase in temperature leads to thermal expansion, altering the fit tolerances and affecting load capacity and precision, while also accelerating lubricant degradation, increasing wear, and reducing bearing service life. Additionally, temperature variations can induce vibrations and noise, alter load distribution, and cause localized stress concentrations and fatigue damage. Therefore, a comprehensive understanding the thermo-mechanical properties of bearings are essential for the stability and efficient operation of mechanical systems. A significant temperature rise of the bearing may lead to (a) changes in lubricating components, (b) deformation, (c) reduction of working clearances between components, (d) increase of local stress and temperature, (e) initiation and propagation of wear, and (f) reduction of the service life of the bearings<sup>1,2</sup>. These changes may lead to premature obsolescence of the bearing components, such as burnout and jamming<sup>3</sup>. Therefore, it is crucial to accurately measure the bearings' temperature field distribution, which is important for the thermal design of double-row angular contact wheel bearings.

Most current literature<sup>4–10</sup> primarily focuses on the numerical and experimental studies of brake rotors for passenger cars and high-performance vehicles. However, there is a lack of research on the non-uniform temperature fields in the bearings under different operating conditions. The core reasons for the complex temperature field are the non-uniformly distribution of internal contact loads and the frictional power consumption. Wan<sup>11</sup> and Harris<sup>12</sup> proposed analytical models for solving the force distribution of a double-row rolling bearing subjected

<sup>1</sup>School of Mechanical and Electrical Engineering, Henan University of Science and Technology, Luoyang 471003, China. <sup>2</sup>Collaborative Innovation Center of Machinery Equipment Advanced Manufacturing of Henan Province, Henan University of Science and Technology, Luoyang 471003, China. <sup>3</sup>Collaborative Innovation Center of Hennan Province for High-End Bearing, Henan University of Science and Technology, Luoyang 471000, China. <sup>4</sup>Suzhou Bearing Factory Co., Ltd, Suzhou 215000, China. ✉email: xiaqidong104@163.com; qiuming@haust.edu.cn

to radial and axial loads. Ji-Won J<sup>13</sup> conducted a fatigue analysis considering the rotating flange of automotive hub bearings. The continuous stress and fatigue analyses were performed by using commercial software. The fatigue performance of the bearing material was obtained through rotational bending fatigue tests, and the analysis results were compared with the test results. Xu<sup>14</sup> reported an analytical model for a double-row angular contact ball bearing to analyze the consequence of ring misalignment on the bearing force distribution and the maximum and average contact forces. Liu<sup>15</sup> reported a dynamic model for double-row angular contact ball bearings to understand the effect of working condition parameters and structural factors on the frictional power dissipation of bearings by construction. Yang<sup>16</sup> established a set of transient thermal equilibrium equations for the temperature field of the shaft system and the iterative process of coupling deformation by applying static mechanics and localized heat source methods proposed for bearings. They found that selecting appropriate clearances, increasing lubricant viscosity, and enhancing air convection can effectively reduce heat generation and thermal deformation. Wen B<sup>17</sup> developed a heat generation model for cylindrical roller bearings based on quasi-static mechanics and thermal network methods, incorporating thermal-mechanical coupling. They analyzed the variations in complex thermo-mechanical characteristics, such as friction torque, contact force, and temperature, during the wear failure of cylindrical roller bearings. Stancekova D<sup>18</sup> performed a transient analysis of a new integrated rotor and hub concept by considering the effects of thermal convection, conduction, and radiation. A testing methodology within a simulated environment is developed for characterization and validation purposes. Additionally, the impact of different blade designs and rotor-hub arrangements on heat transfer mechanisms is investigated. Kim<sup>19</sup> studied the evolution of temperature rise characteristics of ball bearings based on a self-developed temperature rise prediction algorithm, which showed that the volume fraction of the oil phase is an important factor affecting the temperature rise, and better matched with the results of the fluid dynamics simulation by reconfiguring the thermal boundary conditions of Parker's model. Bao<sup>20</sup> constructed a thermal-fluid coupling model of a lubricated ball bearing under the ring based on the CLSVOF model and the Palmgren theory of heat generation, and studied the influence of rotational speed and oil supply speed on the distribution, temperature field evolution and convective heat transfer coefficient of the lubricating oil. A thermal-fluid coupling model of lubricated ball bearing is constructed based on CLSVOF model and Palmgren's thermal generation theory to study the influence of rotational speed and oil supply rate on the distribution of lubricating oil, the evolution of temperature field and convective heat transfer coefficient. Lei<sup>21</sup> constructed a thermal network prediction model for the steady-state temperature field of the under-ring lubricated high-speed ball bearing based on the dynamics and investigated the influence of parameters such as rotational speed, oil supply rate, ambient temperature and so on on the temperature rise of the bearing, and verified the reliability of the model through the finite element simulation. Based on modal testing, the natural frequencies and mode shapes of the main components of the bearings were obtained. To specifically identify bearing defects, a finite element analysis model is established and the deformations of the bearings under applied loads were analyzed.

As the demand for timely and accurate monitoring of bearing operational states increases, researchers are increasingly utilizing advanced sensing technology, such as fiber Bragg gratings for the monitoring and data acquisition of measured physical quantities. And the monitoring of bearing temperature field has been increasingly emphasized by researchers. Existing temperature measurement-based studies primarily monitored the bearing housing or the outer ring of the bearing, which is limited and must be further explored. Jeng<sup>22</sup> mounted resistance temperature sensors on the housing and investigated the law of influence of oil volume, preload, airflow, and speed on bearing temperature. Takabi<sup>23</sup> mounted standard-type K thermocouples on the bearings to compute temperature distribution at the outside ring and lubricating oil. Researchers developed methods to compute multi-point temperature monitoring of bearings for better accuracy. Liu<sup>24</sup> experimentally determined the temperature distribution of the outer ring of a bearing using a Fiber Bragg Grating sensor. Yan<sup>25,26</sup> developed quantum dot temperature sensors, which could compute the temperature of components moving at high speed. However, this process is cumbersome and can only be applied in a controlled environment like a laboratory. Zhou<sup>27,28</sup> conducted a double-row tapered roller multi-measurement point temperature rise test to investigate the effect of operating conditions on temperature distribution. Gao<sup>29</sup> proposed a static model of a double-row tapered roller and obtained the force distribution and kinematic parameters. The temperature distribution of the bearing was investigated through simulation and testing.

There have been fewer theoretical and experimental studies on the thermal characteristics of the double-row angular contact wheel bearings. This paper analyzes the differences in the force distribution and power consumption distribution of the left and right columns of the bearings under different working conditions by constructing a thermal-force coupling model of the wheel bearings. The model investigates the temperature distribution of the bearing through numerical calculations, finite element simulations, and experimental methods.

The innovation of this study is the establishment of a thermodynamic coupling model, which is able to simultaneously consider the thermal coupling effect of bearings under complex working conditions, and the model accuracy is significantly improved compared with the traditional method of analyzing heat or force separately. Meanwhile, in this paper, the fiber grating technology with multiple measurement points is used for the first time to carry out high-precision temperature monitoring of the bearing, which makes up for the shortcomings of the traditional measurement technology, as well as the problem of uneven temperature distribution.

The multi-point fiber Bragg grating measurement technology employed in this study holds significant promise across various industrial sectors, particularly for devices such as machine tool spindles, electric motors, and gearboxes that experience uneven temperature distribution. By utilizing multi-point fiber Bragg gratings, it can optimize equipment performance and facilitate efficient condition monitoring and preventive maintenance.

This approach not only extends the equipment’s service life, but also enables early detection of potential faults, thereby minimizing downtime and enhancing overall production efficiency.

### Heat-force coupling model of automobile wheel hub bearing

This paper considered a double-row angular contact wheel bearings consisting of an outer and an inner ring with an inner flange. The preload was applied using a locknut. The outer ring is considered fixed, whereas the shaft is subjected to a load vector  $F = \{F_x, F_y, F_z, M_x, M_y\}$  after preloading (Fig. 1). The displacement of the inner ring is given by a vector  $d = \{\delta_x, \delta_y, \delta_z + \delta_{pre}, \theta_x, \theta_y\}$ , where  $\delta_x$  and  $\delta_y$  are the radial displacements along the x and y axes, respectively,  $\delta_z$  is the axial displacement,  $\delta_{pre}$  is the preload of the locking nut, and  $\theta_x$  and  $\theta_y$  are the angular displacements of the inner ring due to the torque, respectively.

### Influence of temperature on geometrical parameters of the bearing

*Thermal expansion of bearing components*

Thermal expansion of a rolling body with temperature rise ( $\Delta t_{bk}$ ) is given as Eq. (1)<sup>12</sup>.

$$u_{bk} = \vartheta_b \Delta t_{bk} D_w \tag{1}$$

$\vartheta_b$  is the coefficient of thermal expansion of the rolling element and  $D_w$  is the diameter of the rolling element. The diameter of the rolling body due to expansion is computed using Eq. (2).

$$D'_{wk} = D_w + u_{bk} \tag{2}$$

The thermal deformation of the outer ring raceway groove’s inner diameter ( $D_e$ ) due to a temperature rise  $\Delta t_{ek}$  is computed using Eq. (3).

$$u_{ek} = \vartheta_e \Delta t_{ek} D_e \tag{3}$$

Thermal deformation of the inner ring raceway groove’s inner diameter ( $d_{iL}$ ) and small inner ring’s inner diameter  $d$  due to a temperature rise  $\Delta t_{iL}$  is given as Eq. (4).  $\vartheta_{iL}$  is the coefficient of thermal expansion of the inner ring.

$$u_{iL}' = \vartheta_{iL} \Delta t_{iL} d_{iL}, u_{iL}'' = \vartheta_{iL} \Delta t_{iL} d \tag{4}$$

Thermal deformation of the inner flange’s outer diameter ( $d_{sL}$ ), which is approximately equal to  $d$ , due to a temperature rise  $\Delta t_{sL}$  is given as:

$$u_{sL} = \vartheta_s \Delta t_{sL} (1 + \nu_s) d_{sL} \tag{5}$$

$\vartheta_s$  and  $\nu_s$  are the coefficient of thermal expansion and Poisson’s ratio of the inner flange, respectively.

The radial thermal deformation of the inner ring raceway, when considering the thermal deformation of the inner flange, is obtained by combining Eqs. (4) and (5), is given as Eq. (6).

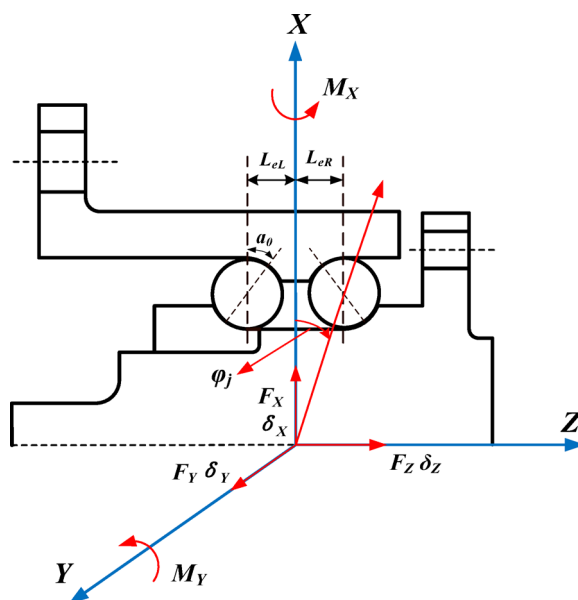


**Fig. 1.** A schematic diagram demonstrating the displacement of wheel hub bearing components subjected to loads and moments in different directions.

$$\begin{aligned}
 u_{iL} &= u'_{iL} + (u_{sL} - u''_{iL})d/d_{iL} \\
 &= \vartheta_{iL}\Delta t_{iL}d_i + [\vartheta_s\Delta t_{sL}(1 + \nu_s) - \vartheta_{iL}\Delta t_{iL}]d^2/d_{iL}
 \end{aligned}
 \tag{6}$$

The increase in diameter of the groove bottom of the raceway on the inner flange of diameter  $d_{sR}$  due to temperature rise  $\Delta t_{sR}$  is given as Eq. (7).

$$u_{iR} = \vartheta_s\Delta t_{sR}(1 + \nu_s)d_{sR}
 \tag{7}$$

$d_{sR}$  is the diameter of the groove bottom,  $\vartheta_s$  and  $\nu_s$  are the coefficient of thermal expansion and Poisson's ratio of the inner flange, respectively.

*Axial and radial displacement of components due to thermal deformation*

The above analysis deduced the displacement due to thermal expansion<sup>30</sup>. The thermal expansion of the outer ring causes the rolling body to be displaced, as shown in Fig. 2(a). The radial expansion component along the normal contact direction is given as Eq. (8). This expansion acts on the rolling body, leading to a relative motion between the rolling body and the inner ring. The displacement along the contact direction is given as Eq. (9)<sup>12</sup>.

$$u_{erk} = u_{ek} \cos \alpha_0
 \tag{8}$$

$$u_{eink} = u_{erk} \cos(\alpha_{ik} - \alpha_{ok})
 \tag{9}$$

The radial and axial displacements of the bearing due to the thermal expansion of the outer ring are given as Eq. (10).

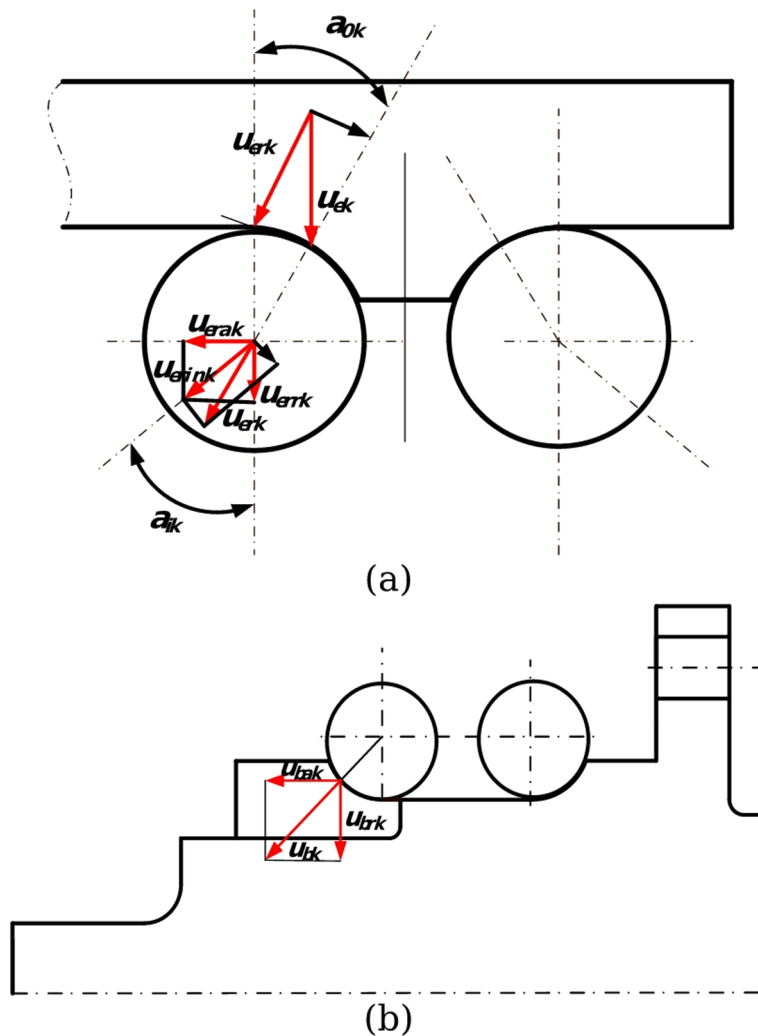


**Fig. 2.** (a) Schematic representation of displacement due to thermal expansion of (a) the outer ring and (b) the rolling elements.

$$\begin{cases} u_{errk} = u_{eink} \cos \alpha_i \\ u_{erak} = u_{eink} \sin \alpha_i \end{cases} \quad (10)$$

Figure 2 (b) depicts the displacements due to thermal expansion of the rolling elements. The axial and radial displacements due to thermal expansion of the rolling elements of the bearing are given as Eq. (11).

$$\begin{cases} u_{brk} = u_{bk} \cos \alpha_i \\ u_{bak} = u_{bk} \sin \alpha_i \end{cases} \quad (11)$$

Accordingly, the axial and radial deformation corrections are computed (Eq. (12)).

$$\begin{aligned} u_{ak} &= u_{bak} + u_{erak} \\ u_{rk} &= u_{ik} - u_{brk} - u_{errk} \end{aligned} \quad (12)$$

### Internal deformation of bearings under thermal coupling

Figure 3 shows the relative position of the rolling body and the center of curvature of the inner and outer grooves after loading and thermal deformation.

The radial ( $U_{rkj}$ ) and axial ( $U_{akj}$ ) distance between the curvature centers of the inner and outer ring grooves in response to thermal force at the bearing can be computed using Eqs. (13) and (14)<sup>12</sup>, respectively.

$$U_{rkj} = \delta_x \cos \varphi_{kj} + \delta_y \sin \varphi_{kj} + m_1 L_{ek} \sin \varphi_{kj} - m_1 L_{ek} \cos \varphi_{kj} + A_k \cos \alpha_{0k} + u_{rk} \quad (13)$$

$$U_{akj} = m_1 \delta_z + m_1 \theta_x r_{pk} \sin \varphi_{kj} - m_1 \theta_y r_{pk} \cos \varphi_{kj} + A_k \sin \alpha_{0k} + \delta_{pre} + u_{ak} \quad (14)$$

$\varphi_{kj}$  ( $j = 1 \dots Z$ ) denotes the bearing position angle,  $A_k$  signifies the center distance of the bearing,  $L_{ek}$  symbolizes the axial distance between the center of the rolling element and the geometric center of the bearing,  $r_{pk}$  indicates the radius of the center circle of the inner ring groove of the wheel bearing, and when  $k = L$ ,  $m_1 = 1$  or when  $k = R$ ,  $m_1 = -1$ .

### Modeling equilibrium conditions

The rolling body's local and inner ring equations can model the bearing equilibrium conditions. Equilibrium conditions due to the rolling body force were first modeled, considering the  $j_{th}$  rolling body for force analysis.

where the force on the steel ball is shown in Fig. 4. When the rolling body is in contact with the inner raceway, it is subjected to (a) the joint action of the inner and outer ring raceway contact force, (b) centrifugal force, and (c) gyroscopic moment—accordingly, Eqs. (15)-(18)<sup>12</sup> can express the equilibrium condition of the  $j$ th rolling body.

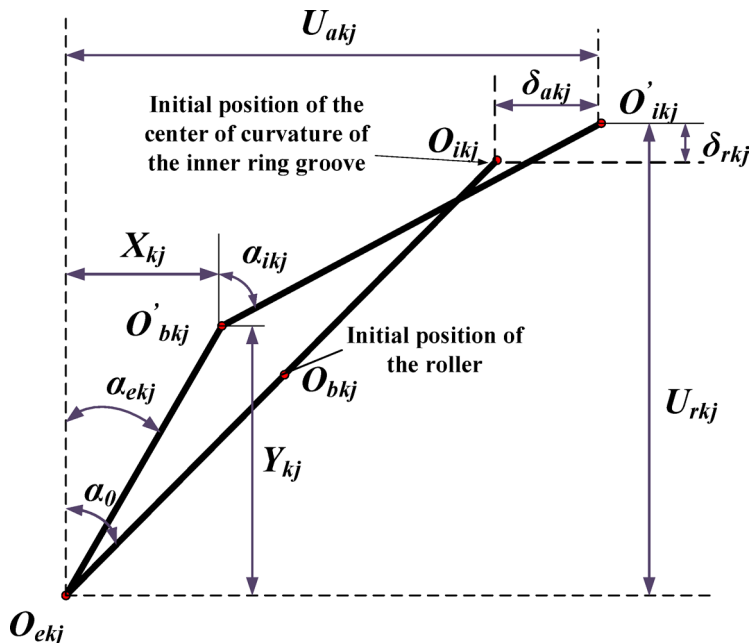


Fig. 3. Internal deformation of bearings.

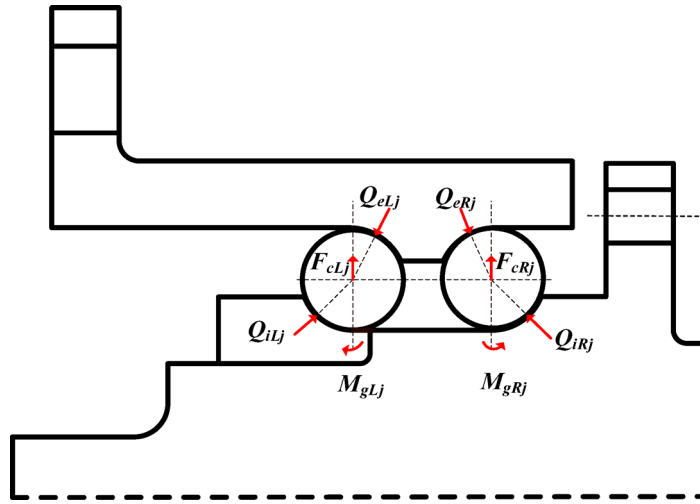


Fig. 4. Rolling body force analysis.

$$Q_{ikj} \sin \alpha_{ikj} - Q_{ekj} \sin \alpha_{ekj} - \frac{M_{gkj}}{D_{wk}} (\lambda_{ikj} \cos \alpha_{ikj} - \lambda_{ekj} \cos \alpha_{ekj}) = 0 \tag{15}$$

$$Q_{ikj} \cos \alpha_{ikj} - Q_{ekj} \cos \alpha_{ekj} - \frac{M_{gkj}}{D_{wk}} (\lambda_{ikj} \sin \alpha_{ikj} - \lambda_{ekj} \sin \alpha_{ekj}) + F_{ckj} = 0$$

$$Q_{mkj} = K_{mkj} \delta_{mkj}^{3/2} \tag{16}$$

$$M_{gkj} = 4.5 \times 10^{-12} D_{wk}^2 n_{skj} n_{mkj} \sin \beta_{kj} \tag{17}$$

$$F_{ckj} = 2.26 \times 10^{-11} D_{pk} D_{wk} n_{mkj}^2 \tag{18}$$

$\lambda_{ikj}$  and  $\lambda_{ekj}$  are the raceway control coefficients. The inner ring raceway control will occur when  $\lambda_{ikj} = \lambda_{ekj} = 1$ . Similarly, the outer ring raceway control will occur when  $\lambda_{ikj} = 0, \lambda_{ekj} = 2$ .  $D_{pk}$  is the bearing pitch circle diameter,  $n_{mkj}$  denotes the rolling body rotational speed,  $n_{skj}$  represents the rolling body rotation speed, and  $\beta_{kj}$  signifies the rolling body rotation attitude angle. When the rolling body gets separated from the inner raceway due to the centrifugal force, the contact and the centrifugal force form an equilibrium state, expressed in Eq. (19) for the  $j_{th}$  rolling body.

$$\begin{cases} Q_{ikj} = 0 \\ Q_{ekj} = F_{ckj} \end{cases} \tag{19}$$

The system for equilibrium of the inner ring has been expressed as Eqs. (20) and (21)<sup>12</sup> were solved using the Newton-Raphson method.

$$\begin{cases} F_x - \sum_{k=L}^{k=R} \sum_{j=1}^Z (Q_{ikj} \cos \alpha_{ikj} \cos \varphi_{kj}) = 0 \\ F_y - \sum_{k=L}^{k=R} \sum_{j=1}^Z (Q_{ikj} \cos \alpha_{ikj} \sin \varphi_{kj}) = 0 \\ F - \sum_{k=L}^{k=R} \sum_{j=1}^Z (m_1 Q_{ikj} \cos \alpha_{ikj}) = 0 \end{cases} \tag{20}$$

$$\begin{cases} M_x - \sum_{k=L}^{k=R} \sum_{j=1}^Z Q_{ikj} \sin \varphi_{kj} (m_1 L_{ek} \cos \alpha_{ikj} - m_1 r_{pk} \sin \alpha_{ikj}) = 0 \\ M_y - \sum_{k=L}^{k=R} \sum_{j=1}^Z Q_{ikj} \cos \varphi_{kj} (-m_1 L_{ek} \cos \alpha_{ikj} + m_1 r_{pk} \sin \alpha_{ikj}) = 0 \end{cases} \tag{21}$$

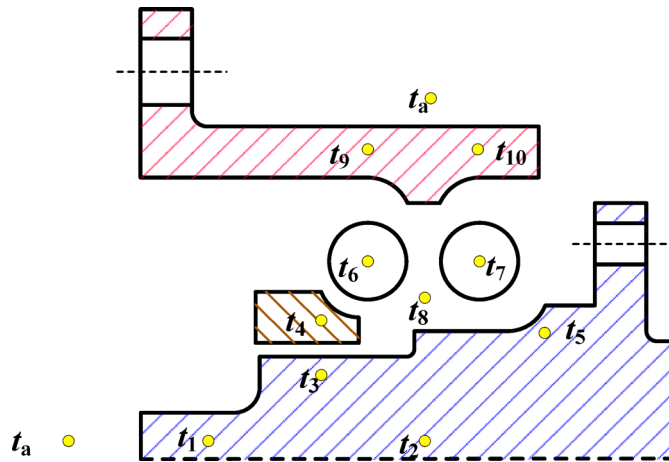


Fig. 5. Arrangement of thermal nodes at the bearing.

Node	Node name	Node	Node name
$t_a$	Ambient temperature	$t_6$	Left column roller temperature
$t_1$	Flange face temperature	$t_7$	Right column rolling element temperature
$t_2$	Flange center temperature	$t_8$	Grease temperature
$t_3$	Inner ring and flange mating surface temperature	$t_9$	Outer ring left column temperature
$t_4$	Inner ring channel temperature	$t_{10}$	Outer ring right column temperature
$t_5$	Flange channel temperature		

Table 1. Bearing temperature nodes.

type	Thermal resistance/(K/W)
Radial conduction thermal resistance	$R_k = \frac{\ln(d_e/d_i)}{2\pi k L_c}$
Radial conduction thermal resistance of the rolling element	$R_k = \frac{1}{\pi k L_c}$
Axial conduction thermal resistance	$R_k = \frac{L_c}{kS}$
Convective thermal resistance	$R_h = \frac{1}{Ah_v}$

Table 2. Formulae for computing the thermal resistance.

### Heat transfer modeling

#### Arrangement of thermal nodes

Temperature nodes and node distribution at the bearing are shown in Fig. 5. The temperature node Settings of each bearing component are shown in Table 1.

#### Calculation of bearing heat generation

The total frictional power consumed by wheel bearings is given as Eq. (22).

$$H_{hub} = H_E + H_S + H_D + H_{grease} \tag{22}$$

$H_E$ ,  $H_S$ ,  $H_D$  and  $H_{grease}$  denotes the friction power consumption caused by elastic hysteresis, spin slip, differential motion of the bearing, and bearing grease, respectively.

#### Heat balance equations

As the temperature considered in this study is below 200 °C, the Effect of thermal radiation is neglected. Therefore, thermal conduction and convection transfer the heat generated during friction. The thermal resistance formulation is shown in Table 2<sup>31–33</sup>.

$k$  is the thermal conductivity of the corresponding material,  $L_c$  is the characteristic length,  $d_e$  and  $d_i$  are the inner and outer diameters of the circular structure,  $S$  is the cross-sectional area,  $A$  is the convective heat transfer area, and  $h_v$  is the convective heat transfer coefficient. The thermal network model’s ambient temperature ( $t_a$ )

is considered constant. The temperature of the ten unknown nodes can be obtained by solving the system of equilibrium equations given in Eq. (23).

$$\left\{ \begin{aligned} 0.5P_{i1} + 0.5P_{e1} &= \frac{t_6 - t_9}{0.5R_{69k}} + \frac{t_6 - t_4}{0.5R_{64k}} + \frac{t_6 - t_8}{R_{68h}} \\ 0.5P_{i2} + 0.5P_{e2} &= \frac{t_7 - t_{10}}{0.5R_{710k}} + \frac{t_7 - t_5}{0.5R_{75k}} + \frac{t_7 - t_8}{R_{78h}} \\ 0.5P_{e1} + 0.5P_{e2} &= \frac{t_9 - t_6}{0.5R_{69k}} + \frac{t_9 - t_{10}}{R_{910k}} + \frac{t_9 - t_a}{R_{9ah}} + \frac{t_9 - t_8}{R_{98h}} \\ 0.5P_{e1} + 0.5P_{e2} &= \frac{t_{10} - t_7}{0.5R_{710k}} + \frac{t_{10} - t_9}{R_{910k}} + \frac{t_{10} - t_a}{R_{10ah}} + \frac{t_{10} - t_8}{R_{108h}} \\ 0.5P_{i1} &= \frac{t_4 - t_6}{0.5R_{64k}} + \frac{t_4 - t_3}{R_{43k}} + \frac{t_4 - t_9}{R_{49h}} \\ 0.5P_{i2} &= \frac{t_5 - t_7}{0.5R_{75k}} + \frac{t_5 - t_3}{R_{53k}} + \frac{t_5 - t_9}{R_{59h}} \\ 0 &= \frac{t_3 - t_4}{R_{43k}} + \frac{t_3 - t_2}{R_{32k}} + \frac{t_3 - t_5}{R_{53k}} \\ 0 &= \frac{t_2 - t_3}{R_{32k}} + \frac{t_2 - t_1}{R_{21k}} \\ 0 &= \frac{t_1 - t_2}{R_{21k}} + \frac{t_1 - t_a}{R_{1ah}} \\ 0 &= \frac{t_9 - t_6}{R_{69h}} + \frac{t_9 - t_7}{R_{79h}} + \frac{t_9 - t_4}{R_{49h}} + \frac{t_9 - t_5}{R_{59h}} \end{aligned} \right. \quad (23)$$

The coupling analysis process of the proposed hydrostatic model of the bearing and its temperature distribution model is as follows: Firstly, the bearing’s kinematic parameters and load distribution are calculated. The results reported the frictional heat generation of each part of the bearing. The heat balance equation is used to solve the temperature of each node. The thermal expansion of the bearing is re-calculated per the calculated temperature of each node to correct the structural parameters. The process is repeated until convergence is recorded.

### Experimental design

#### Design of fiber bragg grating (FBG) sensor package

A box-type encapsulated FBG sensor suitable for the double-row angular contact wheel bearing temperature field measurement is designed to improve the temperature sensitivity and anti-interference of bare FBG sensors. Thermally conductive substrate selection of brass with good thermal conductivity can quickly sense the bearing temperature. The inner cavity is filled with thermally conductive paste. The components of the package include the sealing cover (POM material), the bottom box-type encapsulated sensor (same radius as the bearing outer ring of the arc).

#### Determination of sensor point distribution

A bearing, with parameters given in Table 3, is modeled using ANSYS software (an FEA modeling package). This software is used to compute the temperature distribution accurately under test conditions. Material properties, given in Table 4, are assigned to model components. When the rotational speed is 800 r/min, and the radial and axial forces are 1000 N each.

The temperature of the column near the inner flange connection (referred to as the right column) is higher than that of the other column. According to the temperature distribution diagram of the wheel bearing unit, the temperature rise measurement point will be arranged in the rolling element and the outer ring contact location above, and the left and right columns will be arranged with six measurement points. The measurement point interval is 60°. The arrangement of the temperature rise measurement point is shown in Fig. 6.

In the process of collecting and processing the temperature rise data of the bearing by using fiber grating technology, the collected temperature rise data is processed systematically. In order to get the accurate temperature rise, the data of 10 min after the temperature of the bearing is stabilized is taken and its average

Parameter name	Numerical value
Rolling diameter $D_w$ /mm	15.5
Number of rolling elements Z	12
Distance between the center of the rolling body $L_{bc}$ /mm	23.5
Initial contact Angle $\alpha_0$ /°	40
Coefficient of radius of curvature of inner groove $f_i$	0.515
Coefficient of the radius of curvature of the outer groove $f_e$	0.515
Pitch diameter $D_m$ /mm	65

**Table 3.** Basic parameters of bearings.

Structure name	Material type
Outer flange	55 steel
Inner flange	GCr15
Steel ball	GCr15
Small inner ring	GCr15
Remaining structure	Structural steel

**Table 4.** Model material setup.

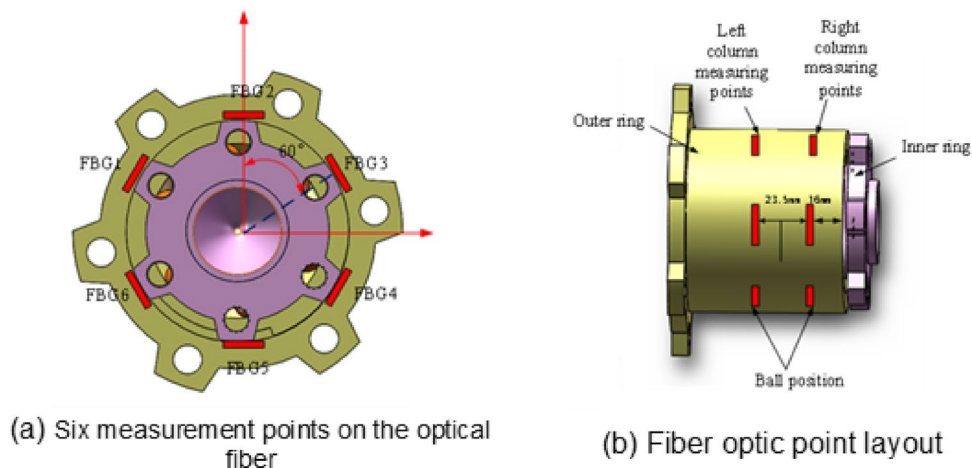


**Fig. 6.** Distribution of temperature rise measurement points.

value is obtained to improve the reliability and accuracy of the data. Ensure that the temperature rise trend can truly reflect the working condition of the bearing.

### Test setup

The bearing temperature rise test setup is shown in Fig. 7, with two sub-systems: (a) forcing device and (b) fiber optic sensing multi-point temperature rise monitoring system. Figure 7(a) shows six components: 1-wheel bearing, 2-package FBG, 3-workpiece connection flange, 4-forcing connection flange, 5-axial forcing force arm, and 6-radial forcing force arm.

The test environment for the bearing was maintained at 28 °C, with the radial loading arm positioned at a certain distance from the bearing's load center to simulate the eccentricity between the tire center and the hub bearing load center. Additionally, the axial loading arm was offset from the hub bearing axis to replicate a tire radius of 375 mm.

The specifications of the fiber grating sensors used in this paper are shown in Table 5.

### Experimental program

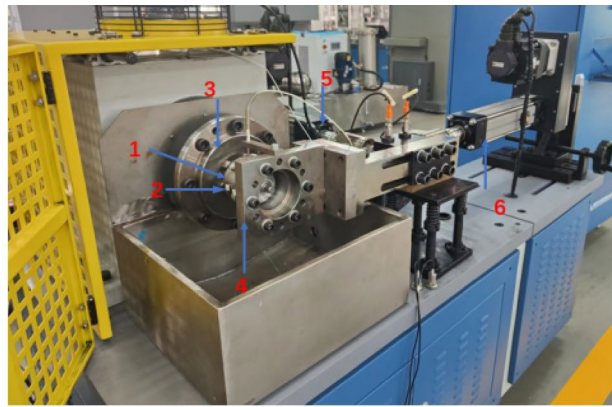
**Experimental materials** Double-row angular contact ball bearings (material and dimensions are provided in Tables 3 and 4).

**Equipment setup** SYJ-LG-NJ bearing life test machine, data converter, fiber Bragg grating, and PC.

### Experimental Procedures:

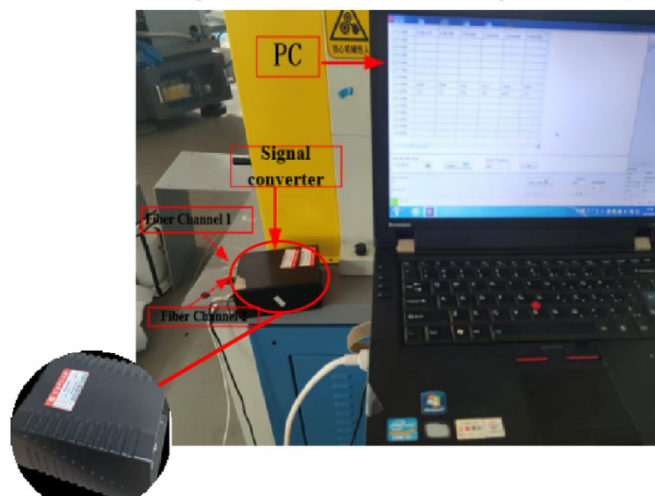
1. Maintain a constant radial load  $F_r = 1000$  N and axial load  $F_a = 1000$  N, while varying the bearing rotational speed.
2. Set the rotational speed at  $n = 800$  rpm, and keep the radial load  $F_r = 1000$  N constant, while varying the magnitude of the axial load.
3. Maintain the rotational speed at  $n = 800$  rpm, and the axial load  $F_a = 1000$  N constant, while varying the magnitude of the radial load.

**Data recording** The sampling frequency is set to 1 Hz.



(a)

(1.the bearing 2. package FBG 3. workpiece connection flange 4. forcing connection flange 5. axial forcing force arm 6. radial forcing force arm)



(b)

Fig. 7. Wheel-bearing multi-point temperature measurement device.

wavelength size(nm)	1535.13	reflectivity(%)	≥ 90%
3dB bandwidth(nm)	0.5–0.6	Grid spacing(mm)	40
Length of grid area(mm)	3	Side mode rejection ratio(dB)	>5

Table 5. Fiber optic grating sensor Specifications.

## Results and discussion

### Influence of working conditions on bearing contact load distribution

#### *Effect of radial force on contact load distribution*

The effect of radial force (1000–5000 N) on the contact load distribution between the left and right columns of the bearing at a constant rotational speed of 800 r/min and the axial load of 1000 N is given in Fig. 8.

As the radial force increases, the contact load distribution in the left and right columns of the bearing changes. For the left column, the contact load gradually increases with the radial force during 1–4 and 9–12 ball numbers. The contact load of the remaining rolling elements decreases with the increase of radial force. Contact load increases with the increase of radial force in the right column during 1–2 and 10–12 rolling elements.

#### *Effect of axial force on contact load distribution*

When the rotational speed is 800 r/min, and the radial force is 1000 N, the effect of axial force (1000–4000 N) on the contact load distribution of the left and right columns of the hub bearing is shown in Fig. 9.

The contact load distribution between the left and right columns of the bearing shows a significant difference with an increase in axial force. In the left column of the bearing, during 4–8 rolling elements, the body contact

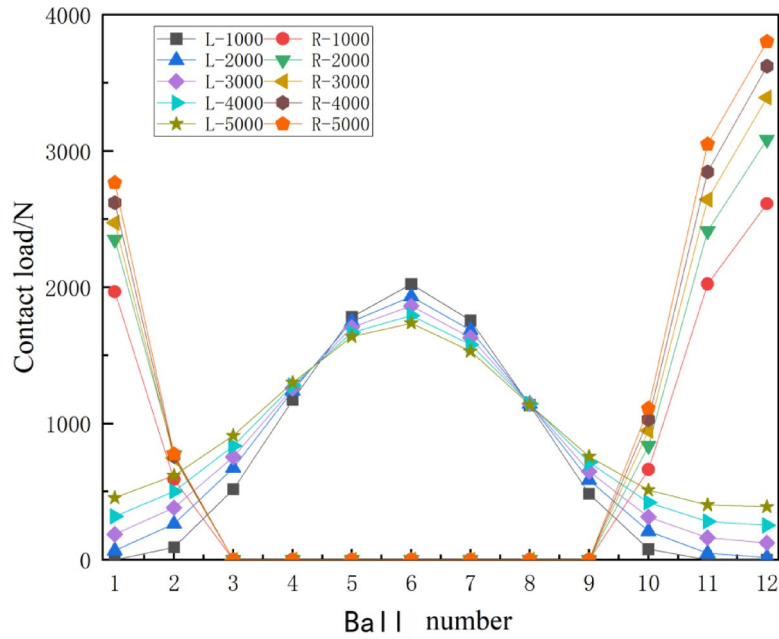


Fig. 8. Influence of radial force on rolling body force distribution.

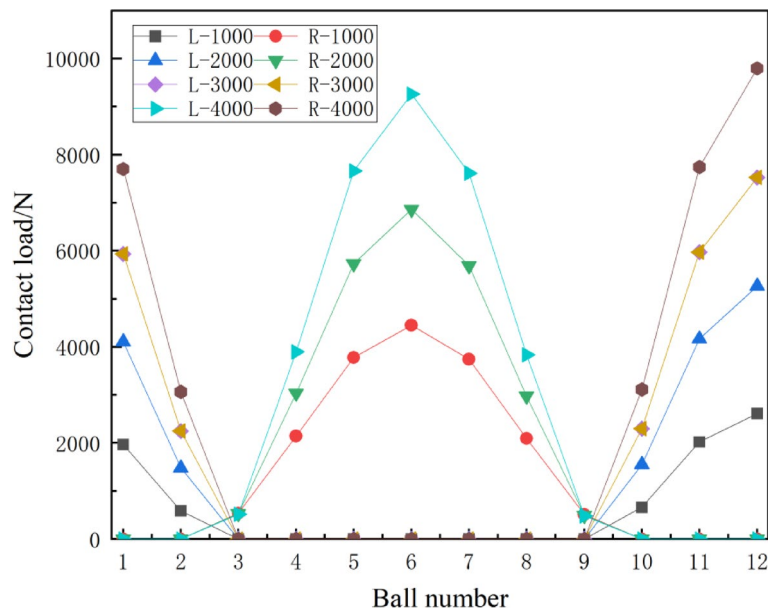


Fig. 9. Effect of axial force on rolling element contact force.

load gradually increases. No changes were noticed during the 2, 3, and 9 rolling elements. The remaining rolling body contact load is zero. The right column of bearings 1–2 and 10–12 rolling body contact load gradually increases; the rest is zero.

**Effect of operating conditions on frictional power consumption in left and right columns**

Based on the results in 4.1, it is noticed that the difference in working conditions leads to a large difference in the load distribution of the left and right columns, so it is necessary to analyze the influence of the load conditions on the heat production of the left and right columns of the bearing.

*(1) effect of axial force on frictional power consumption*

The effect of axial force on friction power dissipation at a rotational speed of 800 r/min and a radial force of 1000 N is shown in Fig. 10(a).

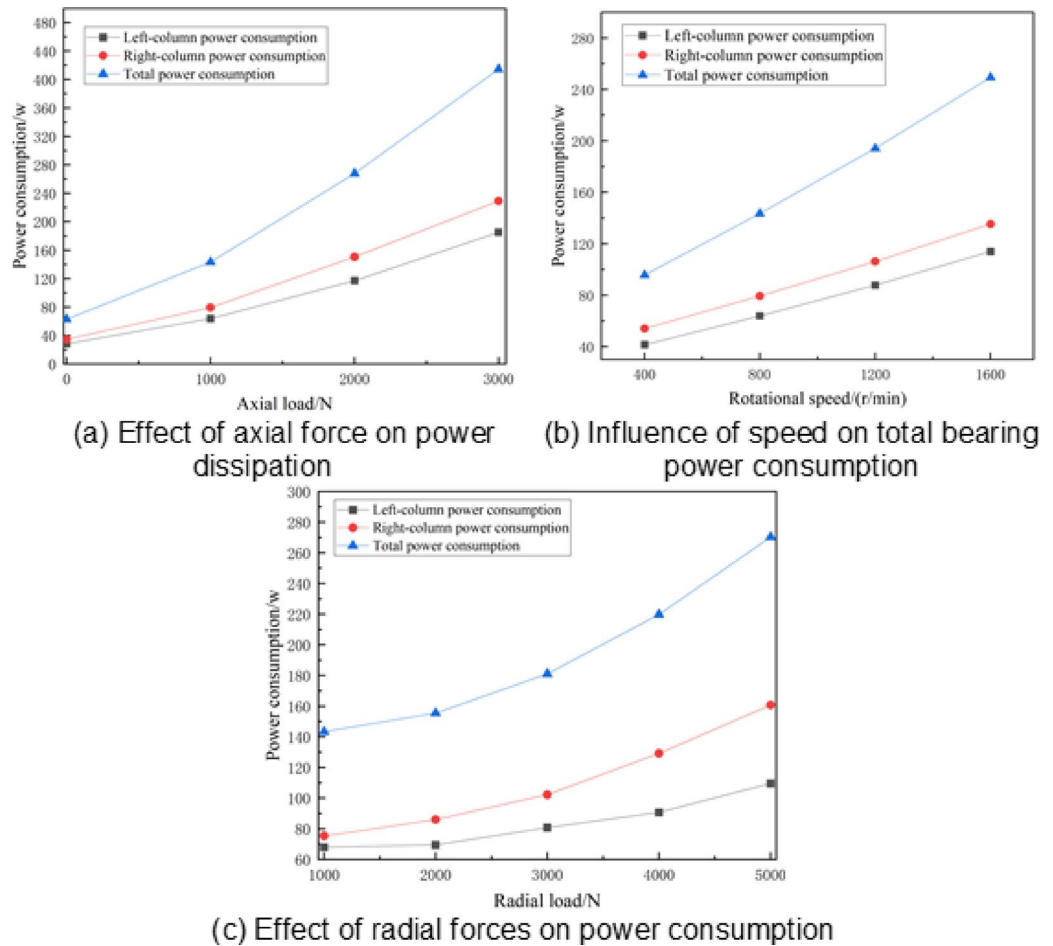


**Fig. 10.** Influence of working condition parameters on friction power consumption.

The heat generation of the bearing increases rapidly, and the rate increases steeply with an increase in axial force. The heat generation of the right column is higher than that of the left column, and the difference increases with the increase of axial force.

#### (2) effect of rotational speed on friction power consumption

The different speed-bearing heat exchange rules are shown in Fig. 10(b) at axial and radial forces of 1000 N each.

An increase in the bearing heat is noticed, following a linear pattern with a relatively high slope, with an increase in rotational speed. In addition, the power consumption of the right column is higher than that of the left column.

#### (3) effect of radial force on frictional power consumption

The effect of radial force on the heat generation of the bearing at a rotational speed of 800 r/min and the axial force of 1000 N is shown in Fig. 10(c).

The bearing heat generation increases gradually, and the rate steeply rises with an increase in radial force. The difference between the power consumption of the left and right columns also gradually increases with an increase in radial force.

### Influence of operating parameters on temperature distribution

The above analysis shows that the contact load and friction power consumption of the left and right columns of bearings are different under different working conditions, which will inevitably lead to the difference in temperature rise of the left and right columns of bearings. Therefore, the thermodynamic coupling model predicts the steady-state temperature rise of the bearings' left and right columns to analyze the difference.

#### (1) influence of axial force on temperature distribution

The influence of the axial force on the temperature distribution at a rotational speed of 800 r/min and radial force of 1000 N is shown in Fig. 11(a).

The temperature rise of the left and right columns shows a piecewise linear increase pattern with an increase in axial load. The slope of linearity increases with an increase in load. The temperature rise of the right column of the bearing is higher than that of the left column.

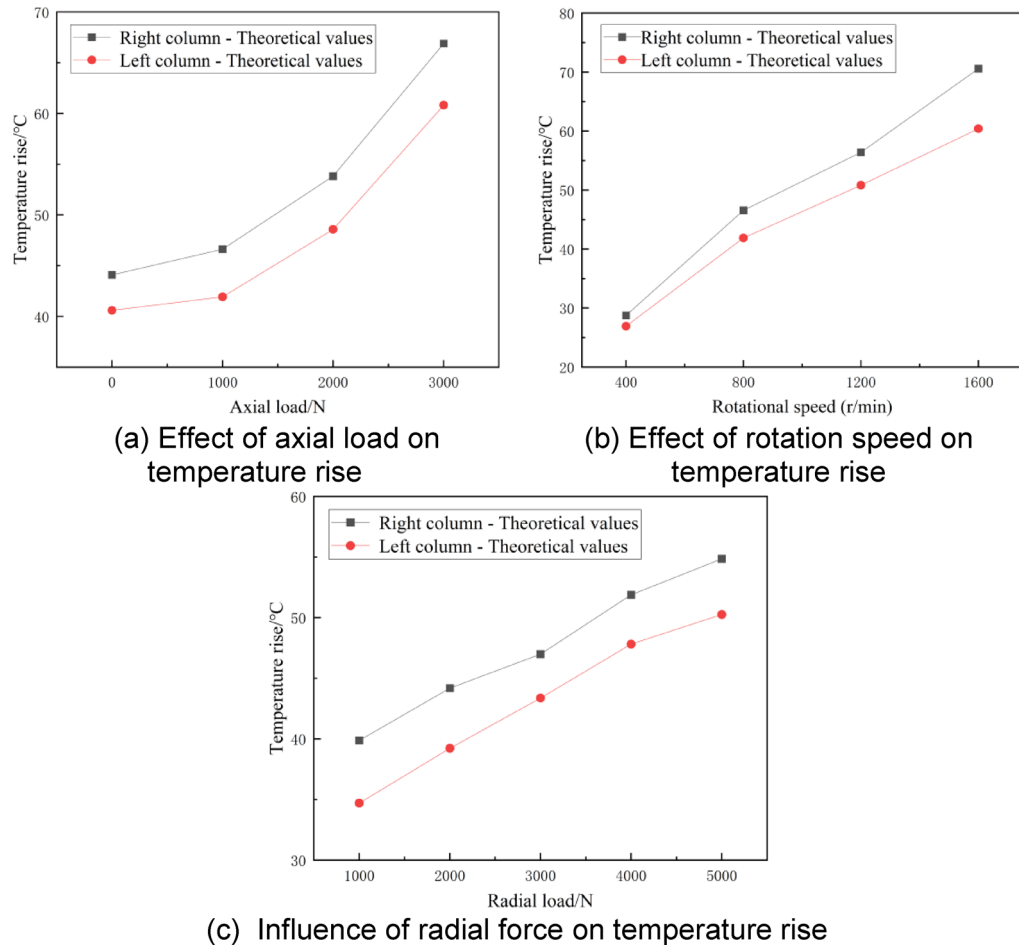


**Fig. 11.** Influence of working condition parameters on temperature rise.

### (2) influence of rotational speed on temperature distribution

The bearing temperature rise rule under different speeds at axial and radial loads of 1000 N each is shown in Fig. 11(b).

The temperature rise of the left and right columns shows a piecewise linear increase in temperature with an increase in rotational speed. The temperature rise of the right column of the bearing is higher than that of the left column, and the temperature difference between the left and right columns gradually increases.

### (3) influence of radial force on temperature distribution

The influence of radial load on temperature rise at a speed of 800 r/min and axial load of 1000 N is shown in Fig. 11(c).

The temperature rise of the left and right columns of the bearing increases gradually with an increase in radial load. Temperature difference in the right column is relatively higher than in the left.

## Experimental test results and analysis of temperature rise

The fiber optic grating sensors are first placed in a temperature control box for calibration. The fiber grating center wavelength and temperature change have a good linear relationship and can complete the measurement of the temperature rise of the bearing (Fig. 12).

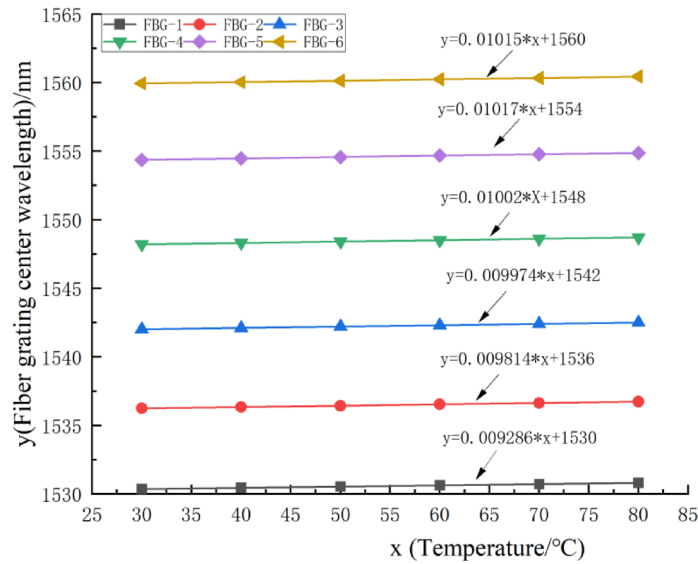
### (1) comparison of theoretical and experimental values

Figure 13(a) shows the theoretically predicted temperature rise under different coaxial loads at a rotational speed of 800 r/min and a radial load of 1000 N was compared with the experimental values.

The trend of the theoretical predicted value is consistent with the measured value with the change in working conditions. The error remains within 10%, indicating the accuracy of the theoretical model.

### (2) temperature rise distribution characteristics

The temperature measurement of each measuring point (station number) is given in Fig. 13(b). A significant difference in temperature rise is noticed along the axial and circumferential direction of the bearing in response to compound loading. Accordingly, studying the influence of working condition parameters on the bearing temperature rise and distribution in more detail is desirable.



**Fig. 12.** Temperature calibration response of experimental setup for fiber optic grating sensors.

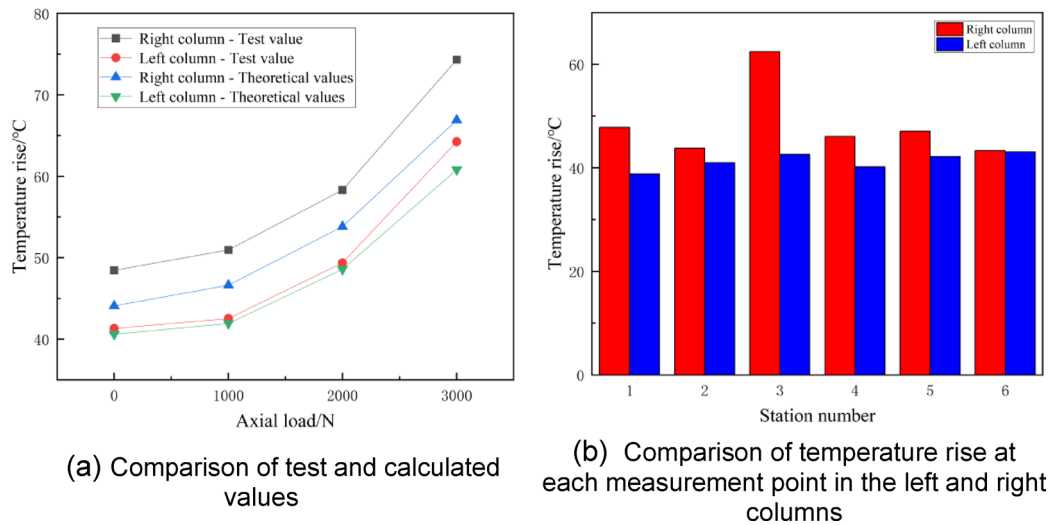


**Fig. 13.** Temperature Rise Comparison.

*Effect of rotational speed on bearing temperature rise distribution*

The temperature rise tests of the bearings at different rotational speeds were carried out at radial and axial forces of 1000 N.

*(1) variation of temperature rise with rotational speed*

Figure 14 shows the results of temperature rise of the bearing with rotational speed under the composite load. The temperature rise of the left and right columns increases rapidly with the increase in rotational speed, and the average temperature rise of the right column of the bearing is higher than that of the left column (Fig. 14-c). The speed increases from 400 to 1600 r/min, and the temperature rise of the left and right columns reaches 66 °C and 76.2 °C, respectively.

*(2) variation of circumferential temperature difference with rotational speed*

Figure 15(a) shows the maximum circumferential temperature difference is between the maximum and minimum values of the measurement points in the left and right columns measured in a steady state.

The results of the circumferential temperature difference with rotational speed show that:

- a. The circumferential temperature difference of the left column of the bearing is less affected by the rotational speed. The rotational speed increases from 400 rpm to 1600 rpm, and the circumferential temperature difference increases to 5.3°C.

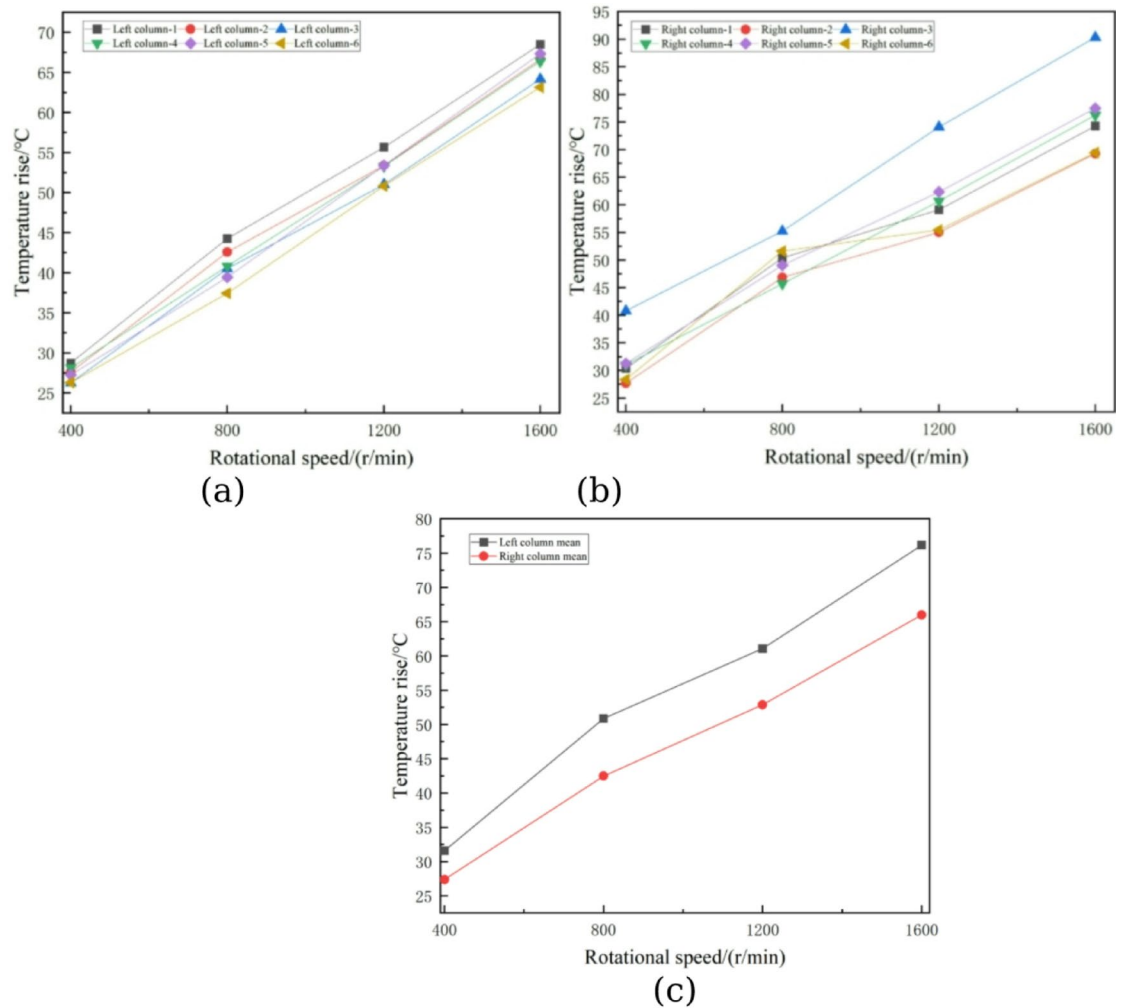


**Fig. 14.** Temperature rise with rotational speed at measuring points of (a) left column and (b) right column. (c) Average rise in temperature at left and right columns.

- b. The circumferential temperature difference of the right column increases with the rotational speed within a range of 400–1600 rpm. It increases slowly, holds at a point, and then linearly increases to 21°C.
- c. The right and left column temperature difference reaches 21°C and 5.3°C, respectively, at 1600 rpm. It indicates the necessity of considering the circumferential temperature difference at high speed.

### (3) variation of axial temperature difference with rotation speed

The difference between the average value of the right and left columns of measurement points in steady state is recorded as the average axial temperature difference. The difference between the maximum value of measurement points in the right column and the minimum value in the left column is recorded as the maximum temperature difference in the axial direction. The results are shown in Fig. 15(b).

The axial temperature rise with the increase in rotational speed shows the following:

- d. The maximum axial temperature difference will increase following a piecewise linear pattern with increased rotational speed. The average axial temperature difference increases linearly, holds between 800 and 1200 r/min, and then increases linearly until 1600 r/min.
- e. The average and maximum axial temperature difference reaches 10.2°C and 27.2°C at the rotational speed of 1600 rpm. It indicates that the axial temperature difference of double-row angular contact hub bearings under composite forcing must be considered when the rotational speed is higher.

### Effect of axial force on hub bearing temperature rise and distribution

A test was carried out to calculate the rise in temperature on the bearing at a rotational speed of 1000 rpm and radial force of 1000 N under different axial forces.

*(1) influence of axial force on temperature rise*

Figure 16 shows the temperature rise variation of the left and right columns with increased axial force in the range of 0–3000 N. The temperature rise was constant, followed by an increasing trend in a linear pattern with increased axial force. With a 3000 N force, the average temperature rise at the left and right columns reaches 64.2°C and 74.3°C, respectively. With the axial force from 0 N to 3000 N, The temperature rise at the left and right columns increases by 22.9°C and 25.9°C, respectively. The temperature rise in the right column is larger than in the left column, mainly because the increase of axial force compressed the right column roller. Accordingly, the right column produces more heat than the left column.

*(2) the influence of axial force on circumferential temperature difference*

The circumferential temperature difference of the right column position of the bearing is larger than that of the left column position, as depicted in Fig. 17(a). In addition, with the increase of axial force, the circumferential temperature difference of the right column has an insignificant change (within 3°C). It shows a zig-zag trend of increasing and then decreasing and then increasing. The circumferential temperature difference of the left column shows a decreasing trend and then increasing (within 6°C), indicating that the axial force's effect on the circumferential temperature difference is insignificant.

*(3) the influence of axial force on the axial temperature difference*

Figure 17(b) shows the average and maximum axial temperature differences at axial forces in the 0–3000 N range. The average axial temperature difference increases with the increase of axial force with increase of axial force. It leads to the generation of frictional power dissipation in the right column component of the bearing, which will be higher than that of the left column. It will result in the consequent increase of the average axial temperature difference of the bearing. The maximum axial temperature difference reaches 27.9°C, when the axial force is 3000 N, and the axial average error reaches 9.8°C. Therefore, the axial temperature difference of the wheel bearing at high axial forces must be considered.

*Effect of radial force on the hub bearing temperature rise and temperature distribution*

Temperature rise tests of the bearing at different radial forces were carried out at the rotational speed of 800 r/min and axial force of 1000 N.

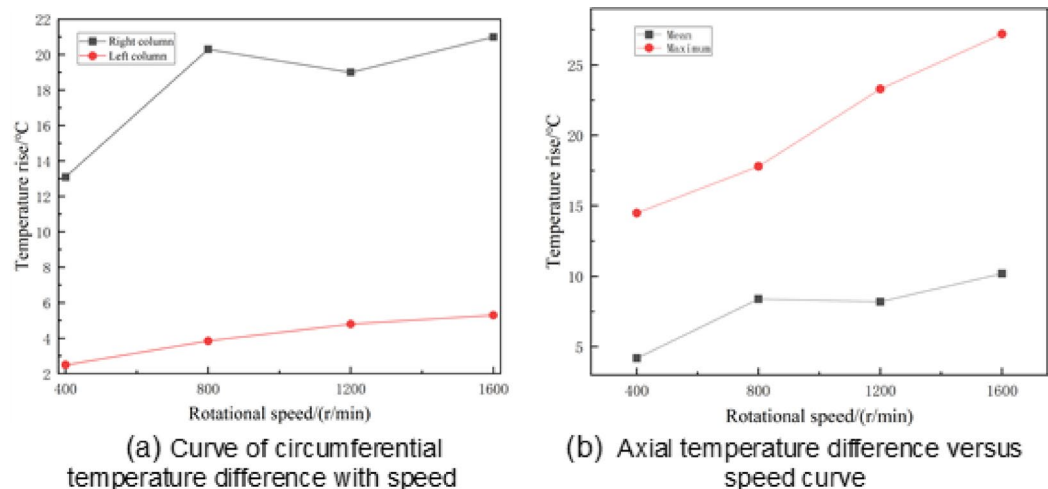
*(1) influence of radial force on temperature rise and distribution*

Figure 18 shows the influence of radial force on the rise in bearing temperature. When the radial force increases from 1000 N to 5000 N, the left and the right columns result in an average temperature rise of 15.98°C and 14.1°C, respectively. The right column has a higher average temperature rise than the left column.

*(2) influence of radial force on the circumferential temperature difference*

Different radial force conditions are considered until the temperature reaches a stable result. The left and right columns of the two fiber strings have respective maximum and minimum values for the difference, the maximum circumferential temperature difference between the left and right columns of the two positions.

Figure 19(a) shows that when the radial force increases in the left column, the circumferential temperature difference is insignificant and maintained at about 2.3°C. The circumferential temperature difference at the right column with increased radial force is relatively complex. The circumferential temperature difference of the outer ring reaches the maximum of 22.18°C at 4000 N load, indicating the necessity for considering circumferential temperature difference at high radial force.



**Fig. 15.** Comparison of temperature rise between left and right columns.

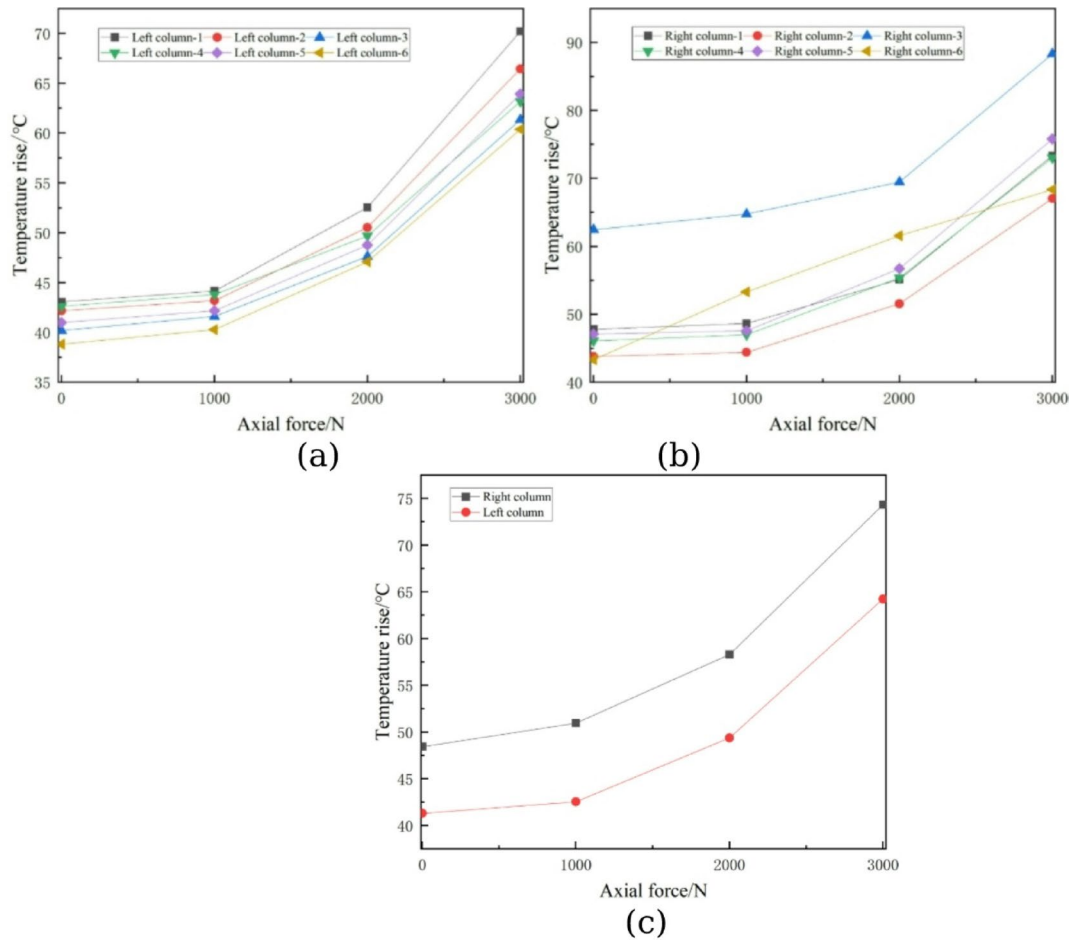


**Fig. 16.** Variation in temperature rises with axial force at measuring points of (a) left and (b) right column. (c) The average temperature rise at different measuring points.

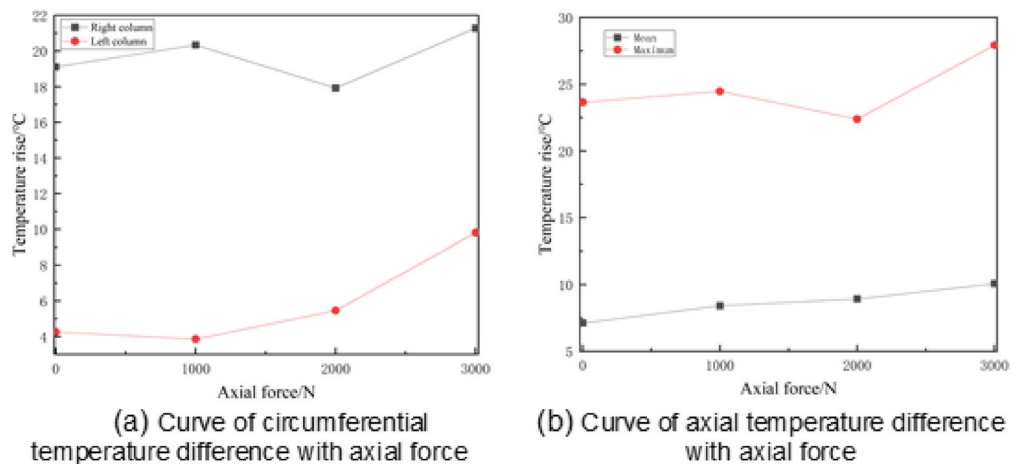


**Fig. 17.** Comparison of temperature rise between left and right columns.

*(3) effect of radial force on axial temperature difference*

The difference between the average values of temperature difference at the right and left columns in steady state is recorded as the average axial temperature difference. The difference between the highest temperature of the right column measurement point and the lowest temperature of the left column measurement point difference is recorded as the maximum temperature difference in the axial direction.

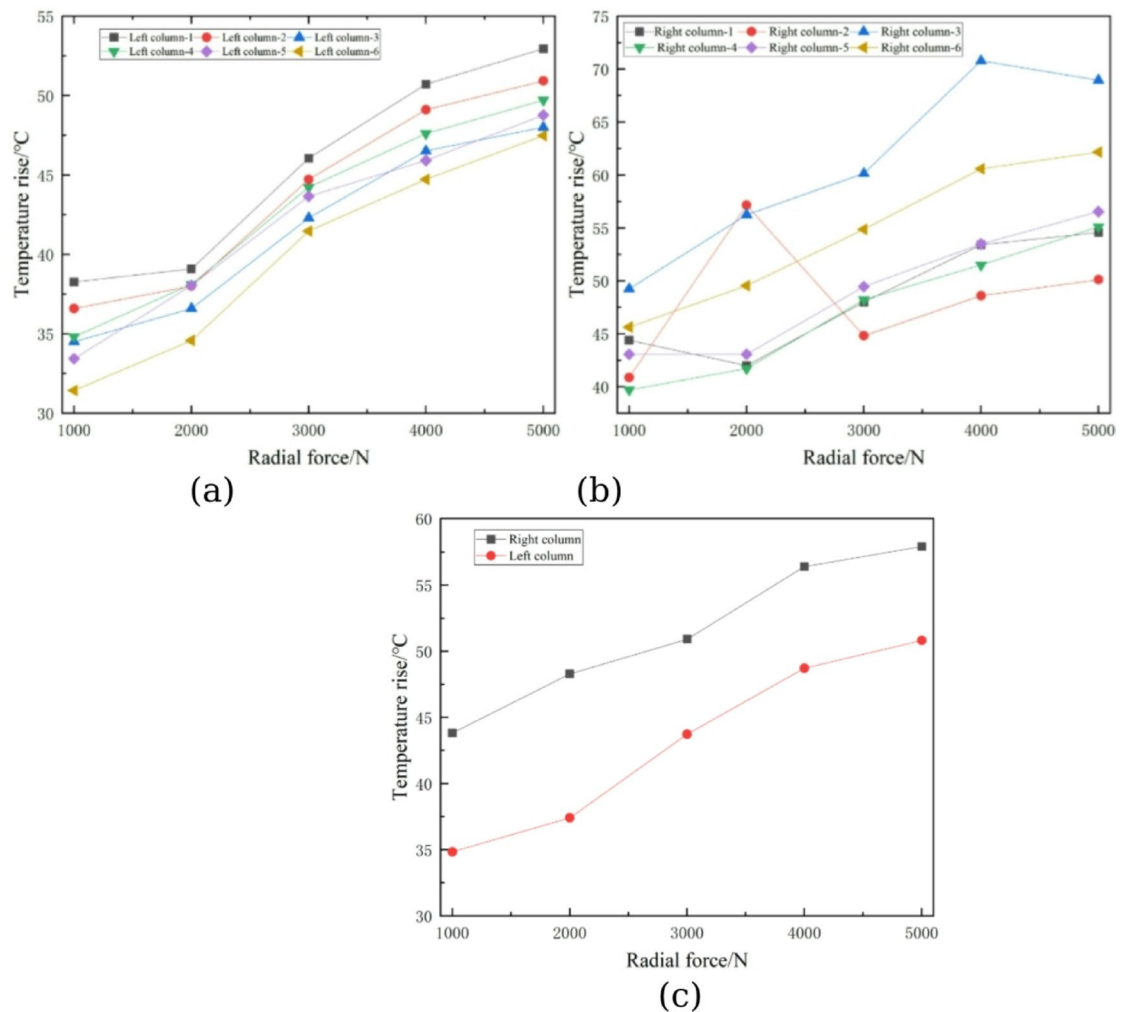


**Fig. 18.** Temperature rise with radial force at measurement points in (a) left and (b) right columns. (c) average values of temperature rise in left and right columns.

The variation in radial force has a complex effect on the axial maximum temperature difference, as depicted in Fig. 19(b). The axial maximum temperature difference ranges between 17.8–26°C with variation of force in a range of 1000–5000 N. In addition, as the radial force increases, the axial average temperature difference first increases, then decreases, and finally tends to be flat. This indicates that the radial force increases to a certain value under the composite force to reduce the axial average temperature difference.

### Analysis of influencing factors of temperature rise and distribution

Based on the above analysis, speed and axial and radial loads will affect the rise in temperature and distribution of hub bearings. Further analysis of influencing factors of the bearing temperature distribution is carried out to determine which operating conditions dominate the temperature distribution. In this paper, the key factors affecting the temperature rise of wheel-hub bearings are analyzed by applying the gray correlation degree analysis model, and the influencing factors that cause changes in the temperature rise of wheel-hub bearings are compared. The temperature rise of the bearing is selected as the reference sequence to calculate the correlation degree between different influencing factors and temperature rise. The greater the correlation degree value, the greater the effect of the factor on bearing temperature rise. The detailed calculation method has been adopted from the literature<sup>34</sup>.

#### Correlation degree results

The influence of the degree of rotational speed, radial load, and axial load on temperature rise in the left and right columns, the average temperature rise, the axial temperature difference, and the left and right columns circumferential temperature difference are analyzed by combining the test data with the grey correlation degree model.

The grey correlation coefficients of the three factors exceed 0.6, indicating that these factors are the main factors affecting the rise in temperature and distribution of wheel hub bearings, as depicted in Fig. 20. Under

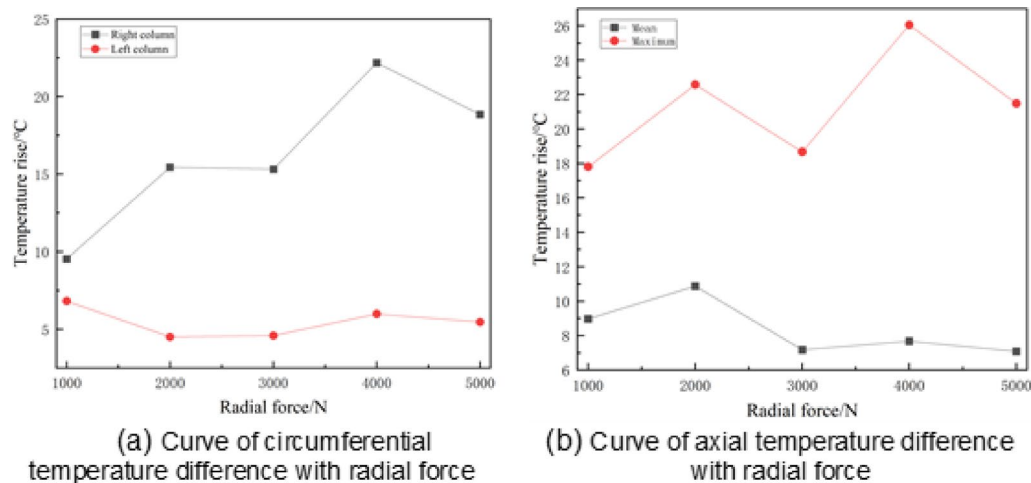


**Fig. 19.** Comparison of temperature rise between left and right columns.

combined loading, the influence degree of speed is highest, followed by axial and then radial force in right and left columns.

## Conclusions

A thermo-mechanical coupling model of double-row angular contact wheel bearing was established to analyze the influence of operating conditions on load distribution, frictional power dissipation, and temperature distribution. A box-packaged FBG sensor was designed for the bearing, with thermal simulation used to determine optimal measurement points. Twelve temperature sensors were arranged to capture the non-uniform temperature field along axial and circumferential directions, validating theoretical predictions. Experimental data further investigated the correlation between operating parameters and temperature rise/distribution. The following conclusions are obtained under compound loading:

- (1) Speed, axial, and radial loads will not ignorably impact the temperature difference between double-row angular contact wheel bearings' left and right columns.
- (2) Under combined loading conditions, rotational speed, axial load, and radial load all significantly influence the circumferential temperature difference of the bearing. Moreover, a notable disparity exists in the circumferential temperature distribution between the left and right rows of the bearing.
- (3) The order of factors affecting the temperature rise of the bearing, axial temperature difference, and circumferential temperature difference is speed > axial force > radial force under compound loading.

## Advantages, limitations, and future directions

This study employs distributed multi-point fiber Bragg grating technology to precisely measure and monitor the temperature distribution and axial and circumferential temperature differences of double-row angular contact wheel bearing, addressing the inaccuracies associated with traditional thermocouple measurements. However, the preprocessing steps for multi-point measurement in practical applications are relatively complex, involving the encapsulation of the optical fibers and the grooving of the bearings. The encapsulation design must effectively protect the optical fibers and ensure measurement stability, while the grooving process is necessary to facilitate the proper functioning of the fibers within dynamic systems.

The future work will focus on simplifying the structure of fiber optic packaging to enhance operational efficiency. Concurrently, infrared cameras will be employed for comparative experiments on temperature data collected from fiber Bragg gratings, aiming to refine measurement techniques and improve accuracy. Furthermore, there are plans to promote distributed multi-point fiber Bragg grating technology in other mechanical systems, such as electric motors and gearboxes, where temperature distribution is uneven. This will be achieved through customized layouts to enhance monitoring capabilities. In addition, by integrating big data analytics, the project seeks to enable real-time monitoring and fault prediction, further enhancing the reliability and safety of equipment while reducing maintenance costs.

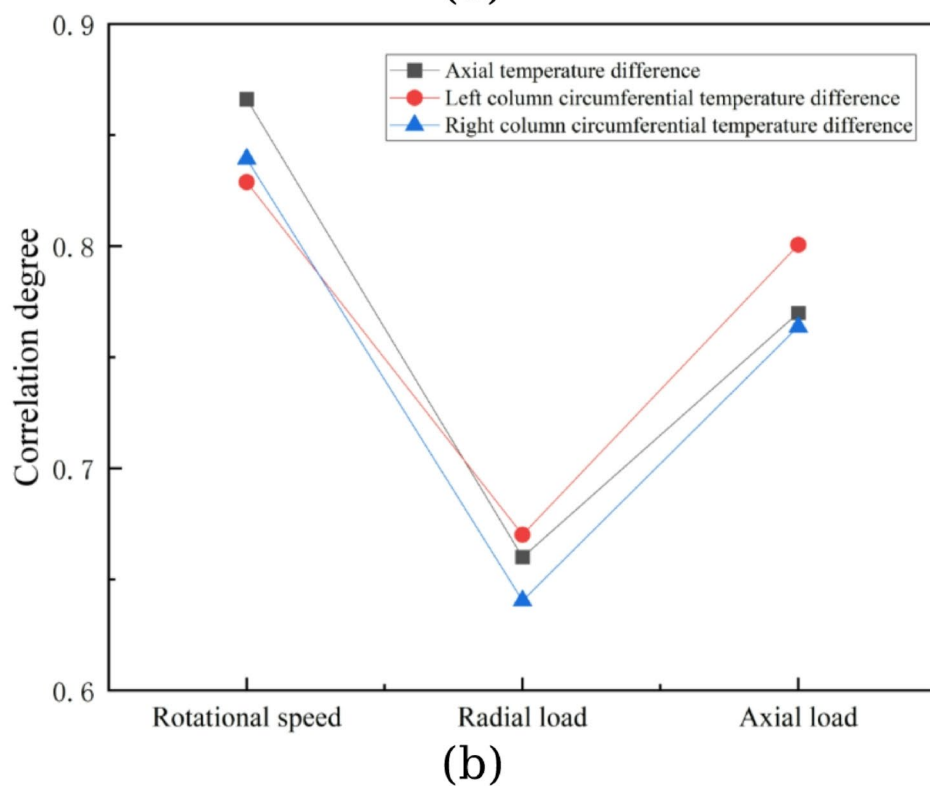
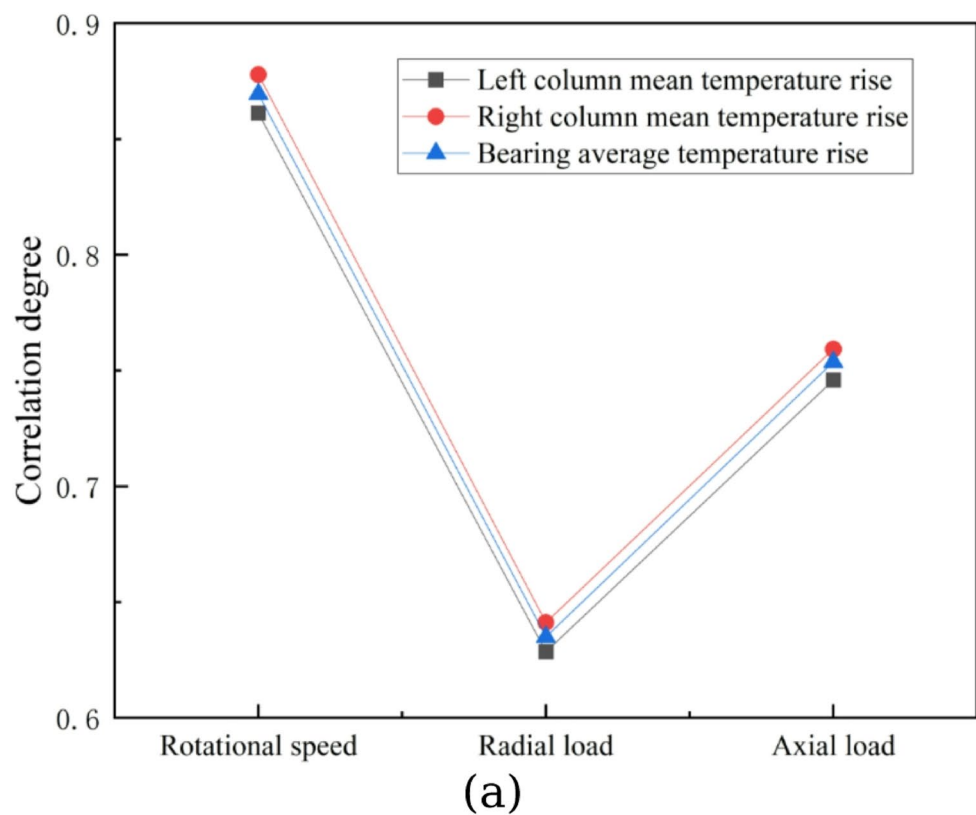


**Fig. 20.** Bearing grey correlation degree between (a) working condition parameters and bearing temperature rise and (b) operating conditions and circumferential temperature difference.

#### Data availability

The datasets used and analyzed during the current study available from the corresponding author on reasonable request.

Received: 9 August 2024; Accepted: 24 June 2025

Published online: 06 July 2025

## References

- Sun, Q. G. et al. *Comparing of Temperatures of Rolling Bearing Under the oil-air Lubrication To the Spray Lubrication [C]*395763–768 (Applied Mechanics and Materials. Trans Tech Publications Ltd, 2013).
- Hamraoui, M. Thermal behaviour of rollers during the rolling process[J]. *Appl. Therm. Eng.* **29** (11–12), 2386–2390 (2009).
- Takabi, J. & Khonsari, M. M. On the thermally-induced seizure in bearings: A review[J]. *Tribol. Int.* **91**, 118–130 (2015).
- Mew, T. Transient thermal response of solid, pinned and highly porous ventilated brake discs. Doctoral Dissertation, (2014).
- Raj, K. T. et al. Numerical investigation of fluid flow and heat transfer characteristics on the aerodynamics of ventilated disc brake rotor using CFD. *Therm. Sci.*, **18**(2), 667–675 (2012).
- Belhocine, A. & Bouchetara, M. Structural and thermal analysis of automotive disc brake rotor. *Arch Mech Eng* ; **61**(1): 89–113. *Therm Sci* 2014; **18**(2): 667–675. (2014).
- Belhocine, A. et al. Thermal analysis of both ventilated and full disc brake rotors with frictional heat generation. *Appl. Comput. Mech.* **8**, 5–24 (2014).
- Shinde, V. V., Sagar, C. D. & Baskar, P. Thermal and structural analysis of disc brake for different cut patterns. *Int. J. Eng. Trends Technol.* **11** (2), 84–87 (2014).
- Yan, H. B., Zhang, Q. C. & Lu, T. J. An X-type lattice cored ventilated brake disc with enhanced cooling performance. *Int. J. Heat. Mass. Transf.* **80**, 458–468 (2015).
- Kiran, C. H. Numerical stimulation of ventilated disc cooling effect. *Int. J. Mech. Eng. Robot Res.* **4** (1), 257 (2015).
- WAN C. *Analysis of Roiling Element Bearings[M]* (Mechanical Engineering Publications LTD London, 1991).
- HARRIS, T. A. *Roiling Bearing Analysis[M]* (John Wiley and Sons Inc, 1991).
- Ji-Won, J. KiWeonKang, seungpyolee. Fatigue analysis for automotive wheel bearing flanges[J]. *Int. J. Precis. Eng. Manuf.* **24** (4), 621–628 (2023).
- Xu, T. et al. Effect of angular misalignment of the inner ring on the contact characteristics and stiffness coefficients of duplex angular contact ball bearings[J]. *Mech. Mach. Theory.* **157**, 104178 (2021).
- Yang, L. Y. et al. Simulation analysis of friction power consumption of Double-row angular contact roller bearing for aeroengine [J]. *J. Mech. Transmission.* **45** (02), 129–135 (2021).
- Yang, C. et al. Thermal characterization of cylindrical roller bearings based on thermal-structural coupling approach. *Adv. Mech. Eng.* **16** (8), 16878132241266458 (2024).
- Wen, B. et al. Thermal Analysis of Cylindrical Roller Bearing Considering Thermo-Mechanical Coupling[J]. *J. Phys. Conf. Ser.* **2185**(1), 012010 (2022).
- D. Staneková, J. Mrázik, Miroslava avodová, et al. Testing the effect of bending moment on wheel bearing Heating[J]. *Manuf. Technol.* **22**(1), 71–79 (2022).
- Kim, D. et al. On heat, temperature, and cavity oil volume fraction of an underace lubricated angular contact ball bearing[J]. *Tribol. Int.* **187**, 108715 (2023).
- Bao, H. et al. Analysis of temperature field and convection heat transfer of oil-air two-phase flow for ball bearing with under-race lubrication[J]. *Industrial Lubrication Tribology.* **73** (5), 817–821 (2021)
- Lei, J. et al. Dynamics-Based thermal analysis of High-Speed angular contact ball bearings with Under-Race Lubrication[J]. *Machines* **11** (7), 691. (2023)
- Jeng, Y. R. & Gao, C. C. Investigation of the ball-bearing temperature rise under an oil-air lubrication system[J]. *Proceedings of the Institution of Mechanical Engineers, Part J: J. Eng. Tribol.* **215** (2), 139–148 (2001).
- Takabi, J. & Khonsari, M. M. Experimental testing and thermal analysis of ball bearings[J]. *Tribol. Int.* **60**, 93–103 (2013).
- Liu, M. et al. Study of the temperature distribution of a machine tool spindle bearing based on FBG quasi-distributed sensing[J]. *Int. J. Adv. Manuf. Technol.* **98**, 263–274 (2018).
- Ke, Y. et al. Research on the temperature measurement principle and realization technology of rolling bearing inner ring based on CdTe quantum Dots. *J. Mech. Eng.* **53**, 134 (2017). (In Chinese).
- Zhang Pan, Y. et al. Use of CdTe quantum Dots as heat resistant temperature sensor for bearing rotating elements monitoring. *IEEE J. Sel. Areas Commun.* **38**, 463–470 (2020).
- Zhou, X. et al. Investigation on thermal behavior and temperature distribution of bearing inner and outer rings[J]. *Tribol. Int.* **130**, 289–298 (2019).
- Zhou, X. et al. Experimental investigation on temperature field of a double-row tapered roller bearing[J]. *Tribol. Trans.* **62** (6), 1086–1098 (2019).
- Gao, P. et al. Theoretical and experimental investigation on thermal characteristics of railway Double-Row tapered roller Bearing[J]. *Energies*, **15** (12), 4217 (2022).
- Zheng, D. & Chen, W. F. Effect of structure and assembly constraints on temperature of high-speed angular contact ball bearings with thermal network method[J]. *Mech. Syst. Signal Process.* **145**, 106929 (2020).
- Yang & Shiming Tao Wenquan. *Heat Transfer [M]. Edition 4* (Higher Education Press, 2006). (In Chinese).
- LI Zhenfeng, SHEN Jinglong, JI Jiawei, et al. Numerical simulation and experimental study on stable temperature field of High-Speed angular contact roller bearing [J]. *Lubr. Eng.*, **46** (01), 45–50 (2021). (In chinese)
- Niu Chen. *Temperature Field Analysis and Life Estimation of the Third Generation Hub Bearing Unit [D]* (Henan University of Science and Technology, 2014). (In Chinese).
- Deng Changcheng, C. et al. Analysis and Test of Influencing Factors of bearing temperature based on Grey Correlation Degree [J/OL]. *Bearing*, 1–10 (2022). (In Chinese).

## Author contributions

Methodology and writing-original draf preparation, data processing and mining, editing, Y.D. and K.H.; M.Q., supervision; Z.Y. and W.Y., data checking.

## Funding

This research was funded by National Natural Science Foundation of China, grant number (No. 52205096) and the Henan Provincial Department of Education. Project (No. 23A460007).

## Declarations

## Competing interests

The authors declare no competing interests.

### Additional information

**Correspondence** and requests for materials should be addressed to D.Y. or Q.M.

**Reprints and permissions information** is available at [www.nature.com/reprints](http://www.nature.com/reprints).

**Publisher's note** Springer Nature remains neutral with regard to jurisdictional claims in published maps and institutional affiliations.

**Open Access** This article is licensed under a Creative Commons Attribution-NonCommercial-NoDerivatives 4.0 International License, which permits any non-commercial use, sharing, distribution and reproduction in any medium or format, as long as you give appropriate credit to the original author(s) and the source, provide a link to the Creative Commons licence, and indicate if you modified the licensed material. You do not have permission under this licence to share adapted material derived from this article or parts of it. The images or other third party material in this article are included in the article's Creative Commons licence, unless indicated otherwise in a credit line to the material. If material is not included in the article's Creative Commons licence and your intended use is not permitted by statutory regulation or exceeds the permitted use, you will need to obtain permission directly from the copyright holder. To view a copy of this licence, visit <http://creativecommons.org/licenses/by-nc-nd/4.0/>.

© The Author(s) 2025